1-1-2016

Droplet Impact on Dry, Superhydrophobic Surfaces with Micro-Scale Roughness Elements

Nadine Boufous

Droplet impact on dry, superhydrophobic surfaces with micro-scale roughness elements

By

Nadine Boufous

A thesis
Submitted to the Faculty of
Mississippi State University
in Partial Fulfillment of the Requirements
for the Degree of Master of Science
in Aerospace Engineering
in the Department of Aerospace Engineering

Mississippi State, Mississippi

December 2016

Droplet impact on dry, superhydrophobic surfaces with

micro-scale roughness elements

By

Nadine Boufous

Approved:

_____

David S. Thompson
(Major Professor)

_____

J. Mark Janus
(Graduate Coordinator / Committee Member)

_____

Adrian Sescu
Committee Member)

_____

Jason M. Keith
Dean
Bagley College of Engineering

Name: Nadine Boufous

Date of Degree: December 9, 2016

Institution: Mississippi State University

Major Field: Aerospace Engineering

Major Professor: David S. Thompson

Title of Study: Droplet impact on dry, superhydrophobic surfaces with micro-scale roughness elements

Pages in Study: 54

Candidate for Degree of Master of Science

Most aircraft accidents are caused by technical problems or weather-related issues. One cause of weather-related incidents is in-flight icing, which can induce negative performance characteristics and endanger the operation of an airplane. Various researchers investigating the problem of in-flight icing have proposed ice-phobic coatings as one viable solution. For this purpose, it is critical to study the behavior of a droplet impact on different types of surfaces. As an alternative to physical testing, three-dimensional numerical simulation using computational fluid dynamics offers a promising strategy for evaluating the effects of surface characteristics. Using the volume of fluid method, three simulations of high-speed droplet impact on superhydrophobic surfaces with and without micro-scale roughness elements, were generated. The simulations showed that, for the roughness configurations considered, the superhydrophobic surfaces with micro-scale roughness elements were significantly less effective at repelling the droplet than the smooth superhydrophobic surfaces.

DEDICATION

This thesis is especially dedicated to my lovely family: my father Lahcen Boufous, my mother Amina Barakat, and my sister Sawssan Boufous. This year would never have been possible without their sacrifices, efforts, and constant support.

ACKNOWLEDGEMENTS

With deep gratitude, I would like to thank my thesis advisor Dr. David S. Thompson of the Aerospace Engineering department at Mississippi State University. He consistently allowed this thesis to be the fruit of my efforts and pushed me to grow as a research engineer. He was always present to steer me in the right direction whenever he thought I needed it and provided me with valuable guidance throughout this year. I would also extend my sincere gratitude to my committee members: Dr. Mark J. Janus and Dr. Adrian Sescu, who graciously accepted to serve on my committee, I am profoundly honored. My sincere thanks also goes to Joey Jones of the MSU HPC for his assistance and advice.

I would like to thank my friends in Starkville and overseas, for their constant support throughout this entire process and for making this year a rich and pleasant experience.

Last but not least, I must express my endless gratitude to my parents and dear sister for providing me with unfailing support and continuous encouragement throughout my years of study and especially this year with my master thesis. This accomplishment would not have been possible without them. Success is in my stride because I have a family like them by my side.

"*At times our own light goes out and is rekindled by a spark from another person. Each of us has cause to think with deep gratitude of those who have lighted the flame within us*".
-Albert Schweitzer

TABLE OF CONTENTS

DEDICATION ii

ACKNOWLEDGEMENTS iii

LIST OF TABLES vi

LIST OF FIGURES vii

NOMENCLATURE ix

CHAPTER

I. INTRODUCTION 1

1.1 Background 1
1.2 Primary contribution 4
1.3 Thesis outline 5

II. LITERATURE REVIEW 6

2.1 Introduction 6
2.1.1 Motivation 6
2.2 Characteristics of the theme 7
2.2.1 Basic splashing 7
2.2.2 Surface characteristics 10
2.2.2.1 Wettability 10
2.2.2.2 Hydrophilic, hydrophobic and superhydrophobic surfaces 10
2.2.2.3 Water repellent surfaces in nature 11
2.2.2.4 Micro-scale roughness elements (MRE) 13
2.2.3 Dynamics of droplet impact on solid surfaces: Experiments 14
2.2.4 Design of ice-free surfaces based on repulsion of impacting water droplets 17
2.2.5 Efficiency of superhydrophobic surfaces regarding icephobicity 18
2.2.6 Numerical simulation methods: Volume of fluid (VOF) 19
2.2.7 Dynamics of droplet impact on solid surfaces: VOF simulations 20
2.3 Summary and conclusion 21

III. COMPUTATIONAL METHODS 23

3.1 Flow solver 23
3.2 Governing equations 24
3.3 Volume of fluid (VOF) implementation 25
3.4 Model for contact line motion 26

IV. RESULTS 29

4.1 Presentation of the cases 29
4.2 Boundary conditions 34
4.3 Case I - Dry, smooth superhydrophobic surface 35
4.4 Case II - Dry, superhydrophobic surface with anisotropic micro-scale roughness elements 40
4.5 Case III - Dry, superhydrophobic surface with isotropic micro-scale roughness elements 43

V. CONCLUSIONS 46

REFERENCES 48

LIST OF TABLES

4.1 Computational time recorded for each case 31

LIST OF FIGURES

2.1 Morphology of droplet impact on dry surface.[18] 8

2.2 Advancing and receding contact angle [19] 9

2.3 Leg of a strider [25] 11

2.4 A-Eye of a mosquito [28] & B- water drops on duck's feather[29] 12

2.5 A-Computer graphic of a lotus leaf surface [31] & B- The Petal effect [32] 13

4.1 Domain of the first simulation - CASE I – 32

4.2 Domain of the second simulation - CASE II – 32

4.3 Domain of the third simulation - CASE III – 32

4.4 Fundamental components of the MRE used for the composition of the domain (CASE III) 33

4.5 Refined Domain 33

4.6 Boundary patches & location of the droplet 35

4.7 Simulation of Case I – Evolution phases of droplet impact on dry, smooth superhydrophobic surface 37

4.8 Droplet Splash 38

4.9 A: Satellite droplet, B: Droplet fingering 38

4.10 Residual droplets 38

4.11 Receding breakup 39

4.12 Retraction of the fluid 39

4.13 Droplet rebound 39

4.14 Simulation of Case II – Evolution phases of droplet impact on dry superhydrophobic surface with anisotropic MRE configuration.....41

4.15 Droplet Fingering 42

4.16 Satellite droplets 42

4.17 Fluid flow patterns.....42

4.18 Incomplete rebound 42

4.19 Simulation of Case III – Evolution phases of droplet impact on dry superhydrophobic surface with isotropic MRE configuration 44

4.20 A:Satellite droplets, B: Droplet fingering 45

4.21 Residual droplets 45

4.22 Complex fluid flow patterns.....45

4.23 Fluid trapped by the cubic posts.....45

NOMENCLATURE

$\propto, \propto_a$	volume fraction of the liquid, volume fraction for the air
θ, θ_0, θ_A, θ_R	contact angle, static/advancing/receding contact angle
μ	viscosity, $N\text{-}s\text{-}m^{-2}$
ρ	density, $kg\text{-}m^{-3}$
σ	surface tension, $N\text{-}m^{-1}$
d	droplet diameter
f_b	body force per unit mass, $N\text{-}kg^{-1}$
P	pressure, $N\text{-}m^{-2}$
t_{wall}	tangent to the wall
T	deviatoric viscous stress tensor, $N\text{-}m^{-2}$
u_θ	velocity scaling parameter for dynamic contact angle, , $m\text{-}s^{-1}$
u_{wall}	velocity parallel the wall, $m\text{-}s^{-1}$
D_0	the initial droplet diameter
V, V_r, V_0	fluid velocity, relative fluid velocity, droplet impact velocity
CPR	cells per radius
MRE	micro-scale roughness element
SCA	static contact angle
VOF	volume of fluid method

Oh	Ohnesorge number
Re	Reynolds number
We	Weber number

CHAPTER I

INTRODUCTION

1.1 Background

When an aircraft passes through a cloud in which the ambient temperature is below the freezing point of water, super cooled droplets come into contact with the surface of the aircraft and freeze. This leads to an accumulation or adhesion of ice to the surface. The resulting ice accretion can induce negative performance characteristics that may alter the operation of an airplane due to carburetor or Pitot tube icing, loss of control, control surface impairment, or engine power loss [1]. Moreover, the aerodynamic drag can be significantly increased by the presence of thin ice accretions while thick accretion can degrade the aerodynamic lift. Therefore, in-flight icing is an important topic relating to air safety.

In order to reduce icing-related incidents, the Federal Aviation Administration (FAA), a branch of U.S. Department of Transportation, provides a national simulator program (NSP) for Flight Simulation Training Device Qualification (FSTD) to evaluate and qualify the engine and airframe icing training tasks [2]. In fact, an aircraft must be able to operate under icing conditions to ensure the safety of its passengers and people present on the ground within the flight perimeter [3]. To this end, there are six types of ice protection systems (IPS): pneumatic de-icing boots, electro-thermal, bleed air, electro-mechanical, the Tecalemit-Kilfrot-Sheepbridge Stokes (TKS) ice protection

system, and passive systems. Note that there is a difference between the de-icing and anti-icing systems; a de-icing system is characterized by the removal of ice from a surface, while an anti-icing system prevents the buildup of ice.

A pneumatic de-icing boot is typically made of rubber and is located at the leading edge of the wings and stabilizers. The accreted ice is fractured when the boot is inflated [4] and the aerodynamic forces remove the ice fragments that have separated from the surface. An electro-thermal system uses resistive circuits placed in the structure of the airframe to generate heat continuously to prevent icing (anti-icing) or occasionally when needed to melt the ice present on the surface (de-icing) [5]. Bleed air is an anti-icing system that works as follow: The hot air from the engine, which is characterized by high pressure and high temperature, is routed into piccolo tubes, i.e., a U-shaped porous tube, that pass through the wing, tail surfaces, and engine inlet in order to prevent icing [6]. Electro-mechanical Expulsion Deicing Systems (EMEDS) are currently used in commercial and military aircraft and use mechanical force to remove the ice present on the aerodynamic surfaces. The actuators i.e., the part of the machine that is responsible for moving a mechanism or a system, are placed under the shell of the structure. The actuators are operated to provoke a shock wave in the surface to dislodge the ice [6]. Other Hybrid Electro-Mechanical Expulsion Deicing Systems couple both EMEDS de-icer and an electrical heating element anti-icer. The ice accreted on the leading edge of the airfoil is averted by the heater while the actuators of the EMED system dislodge the ice accumulated aft of the heated portion of the airfoil [7]. On the other hand, a TKS ice protection system, or weeping wing, prevents ice formation by employing an ethylene glycol-based fluid to coat the critical surfaces of the aircraft [8-9]. Finally, passive

methods are based on the utilization of hydrophobic coatings that are characterized by a high level of water resistance and a natural self-cleaning effect that helps reduce ice accretion [6]. Hybrid systems employ a combination of the various methods [10].

Some of the IPS cited above are ineffective under severe weather conditions. Icing is among the leading causes of numerous aircraft accidents such as the American Eagle Flight 4184 which encountered difficulty to maintain altitude due to a formation of an ice ridge aft of the de-icing boot. This lead the pilots to lose control of the aircraft and it crashed outside of Roselawn, Indiana killing all 68 people on board on October 31, 1994 [11]. Other examples that illustrate the dangers of inefficient IPS include the July 2014 accident involving an MD-83 in the Mali desert that occurred because of the engine icing [12] and the Romanian BN-2A Islander ambulance plane accident caused by a loss of power due to carburetor icing [13].

Moreover, some systems that employ thermal methods can be risky because they involve detection techniques that might be inaccurate. Furthermore, their operation requires considerable energy, which generates additional costs. Over the past ten years, the aircraft industry has opted to look for other solutions such as the use of passive or hybrid methods. The latter are more potentially effective when it comes to ice protection because they prevent ice accretion and adhesion rather than simply removing it and, in addition, consume less energy than the standard methods.

One possible passive solution is the use of ice-phobic coatings and, for this purpose, the dynamics of a droplet impact on dry and wet surfaces needs to be investigated. The contact of a droplet onto a surface is closely related to the surface properties such as wettability and roughness that enhance the surface's efficiency for

water repulsion and thus to ice accretion [14]. In fact, there are various parameters that must be considered for the design of a suitable coating. To this end, there is a need to test the effectiveness of those properties to produce adequate ice-phobic surfaces. As an alternative to physical testing, numerical simulation using computational fluid dynamics (CFD) offers an attractive strategy for estimating surface characteristics.

1.2 Primary contribution

Prior research has revealed a novel mechanism that highlights the importance of dynamic wetting behavior that leads to full retraction and repulsion of impacting water droplets from a cooled superhydrophobic surface before ice nucleation occurs [14]. Based on this finding, the main objective of this work is to study and analyze the behavior of droplet impact on three different surfaces. For this purpose, this investigation will focus on droplet impact on superhydrophobic surfaces with and without micro-scale roughness elements (MRE) that are inspired by superhydrophobic surfaces that occur in nature.

The computational tool used in this investigation is OpenFOAM® 2.3.0 which is an open-source, full-featured CFD flow solver. In order to generate the simulations, its multiphase flow solver interFoam, which employs the Volume of Fluid (VOF) method, was used for all the calculations [15].

For flow visualization, both Ensight 10.1 [16] and Paraview [17] were used progressively from the beginning of the investigation until its end to ensure the proper functioning of the simulations and provide enough information for this research.

1.3 Thesis outline

This thesis begins with a literature review that focuses on the definition of all the important terms related to the topic and presents an overview of prior research. The next chapter, dedicated to the computational methods, covers different elements of CFD calculations as the flow solver, the governing equations, and volume of fluid implementation. The section that follows is the results, where the process of this investigation is explained, including all the techniques used for the mesh generation, the specification of the boundary conditions, the characteristics of the MRE's, and a full description of the results generated by the simulations. The final segment of this thesis gathers an overview of each case, all the conclusions drawn by this investigation and most importantly the effects of MREs on the dry, superhydrophobic surfaces.

CHAPTER II

LITERATURE REVIEW

2.1 Introduction

2.1.1 Motivation

Despite the advances that have been made in aviation technology, an aircraft's surfaces are not totally invulnerable to weather effects. Indeed, an aircraft skin can be strong and especially designed to overcome countless thermal cycles but still remain susceptible to ice accretion under certain meteorological conditions. An ice layer on an aircraft's wing can affect the aerodynamics of the aircraft and diminish its performance. Thus, for a better understanding of this problem and in order to reach a workable solution that can be applied to a large scale surfaces, several efforts investigated the behavior of a droplet impacting a solid, dry surface.

One plausible solution is the following: an inherent surface property with the ability to fend off water droplets that could lead to prevention of icing. This concept led to many experiments that confirmed that highly-ordered, superhydrophobic surfaces can be designed to remain entirely ice-free down to a specific temperature due to their ability to repel impacting water before ice nucleation [14].

2.2 Characteristics of the theme

2.2.1 Basic splashing

While investigating the potential of superhydrophobic surfaces, it is mandatory to understand the dynamics of droplet impact on solid, dry surfaces, especially since they present more complicated flow patterns than wetted surfaces.

The variables that characterize the impact of a droplet are as follows: the initial droplet diameter D_0, droplet velocity V_0, droplet density ρ, droplet viscosity μ, surface tension σ, and measures of the surface roughness and wettability. The surface roughness is usually defined by an average roughness height, R_a and the wettability by a contact angle θ. By using dimensional analysis, these variables can be reduced to only four: a non-dimensional average roughness $R_a{}^*=R_a/D_0$, the contact angle θ and finally Weber and Ohnesorge numbers that will be defined subsequently.

Rioboo *et al.* [18] showed six different droplet spreading regimes as shown in (Figure 2.1): deposition, prompt splash, corona splash, receding break-up, partial rebound and complete rebound. These experiments also illustrate that, during droplet impact on a dry, solid surface, two phases can be distinguished. The first phase (the kinetic phase), is characterized by the fact that the fluid or solid properties do not play a role when the droplet first impacts the surface. During the second phase (the deposition phase), these factors become critical. The first phase consists of the conversion of the kinetic energy into surface energy and is related to the expansion of the droplet over the surface. The second phase is the dissipation of the kinetic energy caused by the interaction of viscous forces between the solid surface and the droplet. In sum, these two results are tightly

related to the kinetic energy present and characteristics of the surface, which can be expressed in term of the contact angle θ.

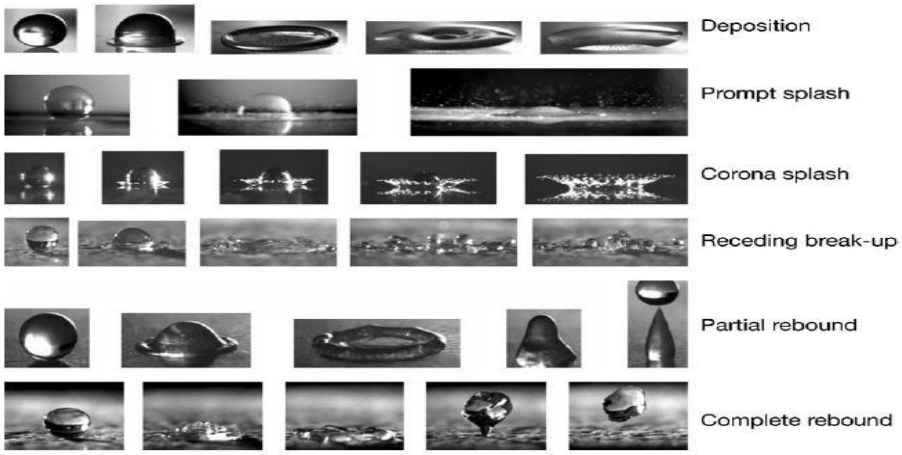

Figure 2.1 Morphology of droplet impact on dry surface.[18]

The two types of contact angle produced by a hysteresis effect (Figure 2.2) are advancing contact angle θ_a and receding contact angle θ_r [19], which can be partially described by using the dimensionless quantities below that indicate if the viscosity effects are significant.

Reynolds number *Re:*

$$Re = \frac{\rho VoD}{\mu} = \frac{inertial\ forces}{viscous\ forces} \tag{2.1}$$

Weber number *We:*

$$We = \frac{\rho Vo^2}{\sigma} = \frac{inertial\ forces}{surface\ tension} \tag{2.2}$$

Or a combination of Re & We, Ohnesorge number *Oh*:

$$Oh = \frac{\mu}{(\rho\sigma D)^{0.5}} = \frac{We^{0.5}}{Re} = \frac{viscous\ forces}{\sqrt{inertial\ forces\ .\ surface\ tension}} \tag{2.3}$$

Note that these non-dimensional parameters cannot fully describe the problem since they do not include any relevant surface characteristics.

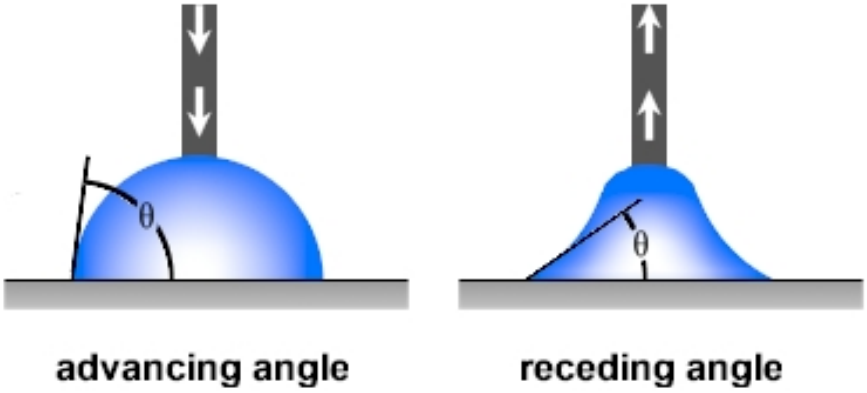

Figure 2.2 Advancing and receding contact angle [19]

Rioboo *et al.* [20] took a particular interest in studying the influence of certain parameters on the contact between a liquid droplet with the solid, dry surface. The experiments were performed using high resolution digital photography and the parameters were varied in a systematic manner. They observed that dimensional similarity of the spreading can only be reached at very early stages of the impact process and that the number of influencing factors increases in later stages. Furthermore, they reached the significant finding that the influence of the surface wettability and roughness is indubitably important. Yarin [21] confirmed this finding and explained this difference more in terms of the dynamics of droplet impact on dry, solid surfaces by highlighting the two important factors that control this phenomenon in his investigation.

2.2.2 Surface characteristics

2.2.2.1 Wettability

The wettability of a surface is the ability of a liquid to maintain contact with a solid surface [22]. There are various degrees of wettability, and they can be differentiated by their contact angle. By this criteria, a surface can be classified into three distinct categories: a hydrophilic surface, which has the physical property of having an affinity for water and characterized by a very low contact angle $\theta < 90°$ (good or complete wetting), a hydrophobic surface, which has the physical property of repulsion of the water and can be distinguished by a high contact angle $90° < \theta < 150°$ (poor wetting), and a superhydrophobic surface that has the same general characteristics as the hydrophobic surface but more enhanced (very poor wetting) and very high contact angle $\theta > 150°$ (see Figure 2.2).

2.2.2.2 Hydrophilic, hydrophobic and superhydrophobic surfaces

Drelich *et al.* [23] enumerated the characteristics of a hydrophilic surface in his research: no long range hydrophobic forces, the free energy of hydration considerably smaller than -113 mJ/m², or a contact angle less than 90 degrees. The most widely known definition is the one that emphasizes the fact that hydrophilic surfaces are characterized by a strong affinity to water.

On the other hand, hydrophobic and superhydrophobic surfaces, as defined above, have the property of water repulsion. Once the droplet hits the surface, it can fully rebound in the shape of a column or a pancake. In the second case, it is highly challenging to make the surface wet as it is extremely hydrophobic.

2.2.2.3 Water repellent surfaces in nature

This ability to reject water can be seen in many organisms in nature such as the strider's legs (Figure 2.3). Indeed, the research conducted by Gao *et al.* [24] showed that a strider's ability to walk and move efficiently on water is due to the high level of hydrophobicity of their legs, which are covered by microscopic hairs.

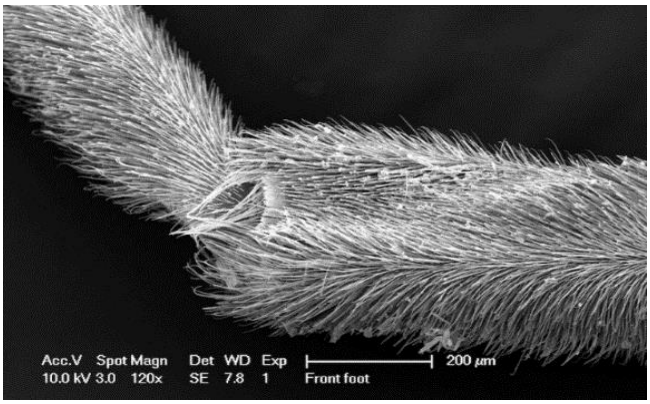

Figure 2.3 Leg of a strider [25]

The eyes of a mosquito (Figure 2.4) represent another example of hydrophobicity in nature. In fact, a study made by Gao *et al.* [26] demonstrated that, thanks to this property of the mosquitoes's eyes, they can remain dry in a humid habitat and therefore maintain clear vision. Liu *et al.* [27] outlined another example of an animal that possess this same property: a duck with its feathers (Figure 2.4). Thanks to their feathers, which show a multi-scale structure, ducks have the ability to repel water droplets and remain as dry as possible.

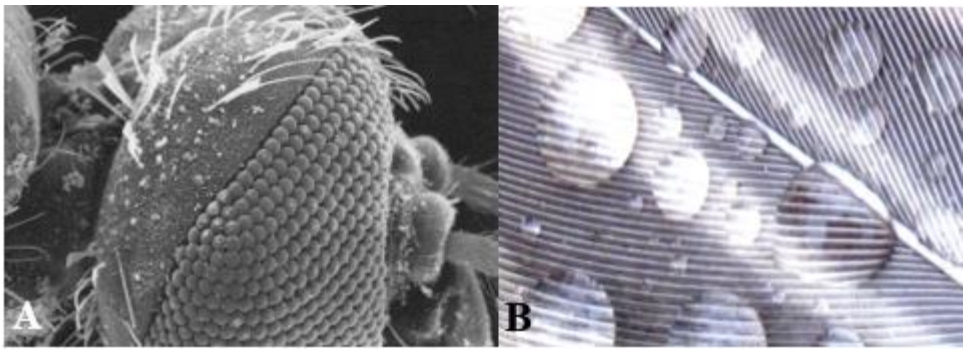

Figure 2.4 A-Eye of a mosquito [28] & B- water drops on duck's feather[29]

Guo *et al.* [30] discussed another well-known example of super-hydrophobicity the Lotus-effect (Figure 2.5). The lotus leaf can emerge from a muddy environment completely clean. This is due to the roughness of its surface which prohibits water droplets from wetting the leaf. The rose petal also demonstrates the ability of water repulsion, but its mechanism works differently. Feng *et al.* [31] investigated this phenomenon and showed that, when a drop of water lands on the rose petal, it balls up and sticks to the surface (Figure2.5). Looking at the petal composition at a microscopic scale, they found that the petal is actually covered with bumps which are in turn covered with folds. The difference between the lotus effect and the petal effect is the fact that the bumps present on the lotus leaf are closely spaced unlike the petal which has well-spaced bumps that cause the droplet to rest on the leaf surface.

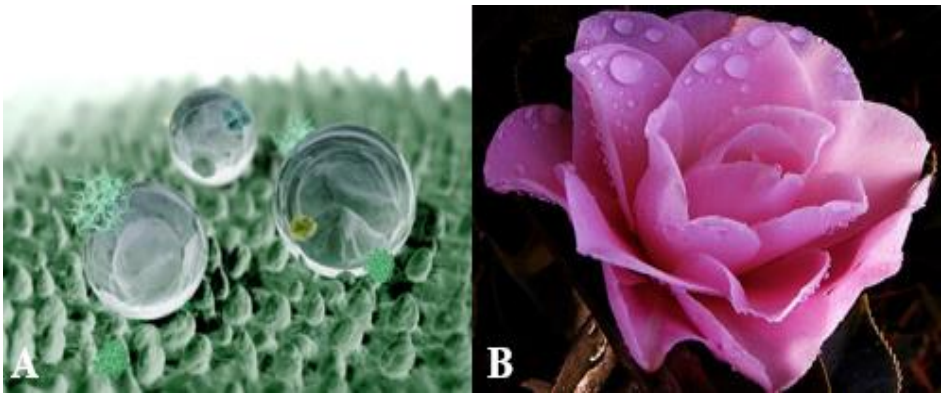

Figure 2.5 A-Computer graphic of a lotus leaf surface [31] & B- The Petal effect [32]

To summarize, these examples present in nature and exhibit something in common, which is the hydrophobic property. This property is present in different forms: chemical surface treatments and also geometrically, such as: bumps, tiny hairs and micro-scale structures, which can be referred to as micro-scale roughness elements (MRE).

2.2.2.4 Micro-scale roughness elements (MRE)

MREs play an important role in determining the interaction between a static droplet and a superhydrophobic surface. For this purpose, the definition and clarification of this term is going to be presented before continuing this investigation.

Scheer & Stover [34] define microroughness as "surface roughness components with spacing between irregularities less than about 100 micrometers." In fact, roughness is a constituent of surface texture with high frequency and short wavelength. It can be measured using the deviation of the normal vector of a real surface from its ideal form. Based on this deviation, the surface can be categorized as a surface that exhibits roughness characteristics or not (smooth).

Several researchers focused on the investigation of a droplet resting on surface with micro-scale roughness elements [35-38]. Yoshimitsu *et al.* [35] showed that, when it comes to some phenomena, such as adherence of snow or raindrops, a proper design of the surface is more effective than an increase in the contact angle. On the other hand, Heydari *et al.* [37] demonstrated that the water freezing delay time is not significantly affected by the surface topography. Overall, the effectiveness of the micro-scale roughness elements have not been established yet.

2.2.3 Dynamics of droplet impact on solid surfaces: Experiments

One of the first studies of droplet impact on a dry surface was done by Worthington [39-41] who focused on droplet fingering and splashing. He used an experimental procedure that is similar to the techniques still used by researchers today. Worthington observed the behavior of both large milk and mercury droplets impacting smooth glass plates. The observations he made include the following: crown formations do not occur; the number of fingers increased with both droplet size and fall height, which implies that they are related; at maximum spread, or soon after, the fingers merge, and more importantly, that fingering was more pronounced for fluids that did not wet the surface than for fluids that did. Engel [42] and Levin and Hobbs [43] noticed that, with increasing surface roughness, the droplets splash upward and form a crown. For impact on a very smooth surface, there is an absence of crown formation.

Based on the observed correlation between surface roughness and droplet impact, Stow and Hadfield [44] demonstrated the existence of a "splash parameter." Splashing occurred when $K = We^{0.5}Re^{0.25}$ was greater than a threshold value Kc, which is strictly a function of the surface roughness. When the roughness of the surface increases, Kc

varies with small values of R_a* and reaches an asymptotic value. Stow and Hadfield observed that it is necessary that the scale of the surface roughness be much smaller than the characteristic height of the fluid sheet to initiate splashing. They suggested that the role of roughness was to initiate an instability in the sheet and noted that the threshold would not apply to a surface roughness comparable to the height of the sheet.

Following the observations of Stow and Hatfield [44], Mundo *et al.* [45] confirmed the asymptotic relationship of splashing with surface roughness through several investigations of small water droplets impacting rough surfaces and noted that the onset splashing was at $Kc = 57.7$. Correlating the data of Stow and Hadfield [44], Mundo *et al.* [45] and Yarin and Weiss [46], Cossali *et al.* [46] obtained the following relationship:

$$Kc^{1.6} = 649 + \frac{3.76}{{R_a}^{*0.63}} \tag{2.4}$$

Watchers and Westerling [48] also correlated the splashing threshold with Weber number We_c and observed the onset of splashing of several different liquids impacting a polished gold surface at $We_c = 80$. Range and Feuillebois [49], also considered the influence of roughness but at low values of Ohnesorge number *Oh* and correlated the onset of splashing with the following expression: $We_c = a\ ln^b({R_a}^*)$, where a and b differed with each liquid-solid combination.

Long before the observation made by Stow and Hatfield [44] regarding the instability initiated by the roughness, Allen [50] took interest in this aspect and published a calculation based on an application of the Rayleigh-Taylor (RT) instability theory. In fact, RT is a fingering instability that occurs at an interface between two fluids of

dissimilar densities in which the lighter fluid pushes the heavier one [51]. RT theory gives the following expression for the fastest growing wavelength:

$$\lambda = 2\pi\sqrt{-\frac{3\gamma}{a(\rho H - \rho L)}} \tag{2.5}$$

with a being the acceleration of the interface, and $\rho H, \rho L$ the density of the heavy and light fluids respectively. In his investigation, Allen [50] estimated the acceleration of the interface to be:

$$a \approx -{V_0}^2/(D_{max}/2) \tag{2.6}$$

with D_{max} being the measured diameter of the droplet, and $N = \frac{\pi D_{max}}{\lambda}$ to estimate the number of fingers visible about the rim of an ink blot.

Bhola and Chandra [52] estimated the acceleration in a different manner as $a \approx -{V_0}^2/D_0$ and presented an analytical expression for the maximum spread, D_{max}, derived from consideration of an integral energy balance [53] and obtained the following expression which was a function of the splash parameter K:

$$N = \frac{We^{0.5}Re^{0.25}}{4\sqrt{3}} = \frac{K}{4\sqrt{3}} \tag{2.7}$$

The previous equation predicted precisely the number of fingers observed after the impact of a wax droplet onto the surface and also gave a good prediction of fingers about molten tin droplets impacting a hot surface [54].

Marmanis and Thoroddsen [55] counted fingers from the blots left by droplets of different liquids impacting a paper surface and obtained the following correlation:

$$N \approx (We^{0.25}Re^{0.5})^{0.75} \tag{2.8}$$

Comparing the data obtained with that of Worthington [41], they observed that there is a significant discrepancy, which might be explained by the difference in the wettability of mercury on glass compared to the liquids they used on a paper surface.

Finally, Kim *et al.* [56] used an RT-based linear perturbation theory to analyze the stability of the layer of fluid that jets radially outward beneath an impacting droplet right after contact. Their results predict the variation of the fastest growing wavelength with time. For appropriate assumptions of when the fingers first appear, the model yielded estimates of N in line with experimental observations [57].

2.2.4 Design of ice-free surfaces based on repulsion of impacting water droplets

Hydrophobicity and superhydrophobicity observed in nature inspire mechanisms of de-icing that work in various ways either mechanically, pneumatically, or chemically. Xiao *et al.* [58] investigated the development of durable surfaces that can prevent icing, where airstream shear forces remove the ice accretions. Their work provides a means to predict the anti-icing performance of several nanocomposite coatings under in-flight environments.

Mishenko *et al.* [14] focused on the behavior of dynamic droplets impacting supercooled nano-structured and micro-structured surfaces. Their experiments showed that superhydrophobic materials can be totally ice free between -20° to -30° C, thanks to their ability to fend off impacting droplets before the nucleation phase. Ice below this temperature can be easily removed, while ice accretion is prevented above this temperature. The design of an ice-free coating can be done by bringing together all major factors as heat transfer, wetting characteristics, and the nucleation phase. Starting from this investigation, they conclude that the most effective ice-free coating would be

hydrophobic polymeric coating with closed-cell micro-structured surfaces. Indeed, these surfaces have potential because the micro-structures are easy to replicate using large scale manufacturing.

Sharing the same perspective, the investigation of Cao *et al.* [55] led to a focus on the performance of superhydrophobic coatings for anti-icing applications. They used nanoparticle-polymer composites to prevent ice formation at the time of impact of the supercooled droplets. Cao *et al.* found that the capability of those composites depends also on the size of the particles on the surface. In fact, they concluded that the critical size is dissimilar to the critical size that determines the characteristics of these surfaces; therefore, it is necessary to acknowledge the surface morphology before determining if the superhydrophobic surface indeed has anti-icing properties.

2.2.5 Efficiency of superhydrophobic surfaces regarding icephobicity

Jung *et al.'s* [60] investigated superhydrophobic surfaces to determine if they are truly the best for icephobicity. They based their result on the delay of freezing water on different surfaces-untreated and coated from hydrophobic to superhydrophobic. Supercooled, micro-droplets of water were placed on different surfaces and were observed until freezing occurred. The surfaces with nanometer scale roughness and higher wettability showed unpredictably long freezing delays unlike the other superhydrophobic surfaces with higher roughness and lower wettability.

Jung *et al.'s* [60] observations revealed an unseen atmospheric-pressure, subfreezing temperature regime for liquid on liquid bounce, which led them to reformulate the classical heterogeneous nucleation theory that predicts the observed freezing delays. Thus, the results suggest that ice repellent design of surfaces must

improve the two important factors of wettability and roughness. Therefore, the results of this experiment pointed out that the choice of the best icephobic surface has to be based on a complete examination of both factors: freezing delay and ability to fend off liquids.

2.2.6 Numerical simulation methods: Volume of fluid (VOF)

While simulating any given problem involving flows with moving interfaces, there are a number of techniques that can be used: The Volume of Fluid method (VOF) [61], the Front Tracking method [62], the Level Set method [63], and the Lattice Boltzmann model [64].

Hirt and Nichols [61] defined VOF as a method that is based on the idea of a fluid volume fraction and uses a numerical technique for detecting and locating the free interface. In turn, Gouez *et al.* [65] gave a simple explication of this technique as follows: $\propto$ is a function that represents the volume fraction fluid in each cell. If the value is a zero, it means that the cell does not include the fluid. In contrast, when the value differs from zero, it means that the cell contains fluid. The free surface is defined by cells whose value is between zero and one (following the condition that the overall sum of volume fraction is equal to one).

The following transport equation controls the evolution of the function volume fraction field

$$\frac{\partial \propto}{\partial t}+u\frac{\partial \propto}{\partial x}+v\frac{\partial \propto}{\partial y}+w\frac{\partial \propto}{\partial z}=0. \tag{2.9}$$

In equation (2.9), t represents the physical time, (u, v, w) are the Cartesian components of the velocity and (x, y, z) the Cartesian coordinate system. The donor-

acceptor method [64] is used to calculate the flux of $\propto$ over the sum of all the faces of a cell, which represents the evolution of $\propto$ in each cell.

2.2.7 Dynamics of droplet impact on solid surfaces: VOF simulations

Many numerical studies simulating droplet impact have dealt with the two-dimensional or axisymmetric problem of a droplet impacting normal to a smooth surface. The axisymmetric assumption inhibits the consideration of flow in azimuthal direction and therefore the consideration of splashing and fingering. To overcome this problem, full three-dimensional models of droplet impact have recently been performed. In the investigation of Bussman *et al.* [66], a numerical model was used to simulate the effects of droplet impact on a solid surface, using a methodology for velocity perturbation of the fluid near the solid surface shortly after impact. Simulation results were presented for the impact of water, heptane and molten tin droplets and compared with images of corresponding impacts. The results of this investigation were based on the three-dimensional model of Bussman *et al.* [67] and simulation results consistently agreed with the experiment. The results of this investigation demonstrated that the contact angle plays a major role for water and heptane and that the expression that can predicts the behavior of the molten tin may be valid only for impacts characterized by a relatively low value of the Ohnesorge number.

The impact of a droplet on a solid, dry surface has been experimented by using VOF simulations by Gunjal *et al.* [68]. The main purpose of this study was to highlight the key issues related to droplet spreading over the surface. A high speed digital camera was used to capture the progression of the droplet while impacting flat surfaces (glass & Teflon). The experimental data on the dynamics of the droplet impact were classified

over a range of Reynolds and Weber numbers. The simulation consisted of the use of CFD model based on VOF method. During the comparison of the experiment and simulation, they concluded that the results were satisfying. The major strength of the simulations is the fact that they provide more details about the interaction of droplets with the surfaces used in the experiment. Finally, the modeling of these droplets on a dry, solid surface can be reliable; however, according to Yarin [41], there are still some gaps concerning the boundary conditions to be implemented at the moving contact line and the transition from the spreading to the receding stage where the contact line is arrested.

Numerical investigations of droplet impact were performed by Burtnett [69]. Her work targeted droplet impact on both dry and wetted superhydrophobic surfaces using a VOF flow solver. More precisely, she investigated the effects of droplet impact on dry and saturated surfaces with structured, MREs and on dry, smooth surface. Axisymmetric domains were employed and those latter produced acceptable results for smooth, dry surfaces. In contrast, the results for the surfaces with MREs provided inconclusive findings and, for this purpose, it was determined that three-dimensional simulations are recommended in order to properly predict behavior of droplets impacting surfaces with structured MREs.

2.3 Summary and conclusion

This literature review helped gather enough information about previous investigations in this research area. It also demonstrates that superhydrophobic surfaces offer a potential solution to overcome the problem of ice accretion and the importance of both wettability and roughness. Moreover, it also shows that investigations done on static

droplets resting on rough superhydrophobic surfaces did not established the effectiveness of the MREs.

Several two-dimensional simulations have been employed to study droplet behavior on superhydrophobic surfaces while three-dimensional simulations were just starting to be performed. For this purpose, the next step would be to investigate high speed droplet impact on superhydrophobic surfaces with MREs using three-dimensional CFD simulations. The two MRE configurations considered consisted of anisotropic channels, which were selected to mimic the hair on the strider legs (Figure 2.3) and the duck feathers (Figure 2.4 B), and isotropic posts, which were chosen to mimic the mosquito eye (Figure 2.4 A) and the lotus leaf (Figure 2.5 A).

CHAPTER III

COMPUTATIONAL METHODS

3.1 Flow solver

This investigation used OpenFOAM®2.3, released on 17th February 2014, for all numerical simulations. Open Field Operation and Manipulation (OpenFOAM) is an open source CFD toolbox managed by the OpenFOAM Foundation [15]. The toolbox includes a wide range of features, with numerous options, that can be employed to solve different problems ranging from molecular dynamics to electromagnetics problems. It also has several utilities for mesh generation and manipulation than can be used depending on the nature of the problem.

In this effort, interFoam [15], which was first developed by Rusche [70] and then modified by OpenCFD, Ltd. [71], was used to generate simulations for a liquid droplet impacting a dry surface in the presence of still air, using the VOF method. For problems involving two immiscible fluids, the VOF method solves the phase fraction equation for each phase in order to guarantee conservation, boundedness, and the accuracy of the solution, especially when the problem is dealing with two fluids with very different densities. In this investigation, the two fluids considered are the quiescent air and the water droplet.

3.2 Governing equations

The governing equations, continuity and momentum, are solved simultaneously with the transport equation for the volume fraction $\propto$

$$\nabla . V = 0 \tag{3.1}$$

$$\frac{\partial(\rho V)}{\partial t} + \nabla(\rho VV) = -\nabla \mathrm{P} + \nabla . \mathrm{T} + \rho f_b \tag{3.2}$$

$$\frac{\partial \propto}{\partial t} + \nabla(\propto V) = 0 \tag{3.3}$$

where V is the velocity shared by the two fluids, ρ is the density, P is the pressure, T is the deviatoric stress tensor and f_b is the continuum surface force (CSF) [72].

For numerical computation, interFoam uses a cell center-based, finite volume method on a fixed grid. The pseudo-transient (PIMPLE) algorithm, which is a hybrid algorithm that combines the pressure-implicit split-operator (PISO) and semi-implicit method for pressure-linked equations (SIMPLE) algorithms [73-74], is used to couple both pressure and velocity in unsteady flow.

In order to ensure boundedness and consistency of computed scalar fields, the interFoam solver utilizes the multidimensional universal limiter for explicit solution (MULES) method [75]. In OpenFOAM 2.3, a new, semi-implicit variant of MULES is used where it associates operator splitting with application of the MULES limiter to an explicit correction rather than to the complete flux. A time step of the algorithm starts with the application of an implicit predictor step before constructing an explicit correction to which the MULES limiter is applied. This semi-implicit method is faster than the explicit method used in the previous variant of MULES.

The finite volume method is used to discretize the governing equations while the transient and source terms are discretized following the midpoint rule and then integrated over the cell volume. The time derivative terms are discretized using a first-order implicit Euler method and the spatial derivative terms are transformed to integrals over the surface of each cell with a second-order Gaussian integration. The integration is obtained adding up all the values of cell faces. In order to precondition the pressure equation, a diagonal incomplete-Cholesky (DIC) preconditioned conjugate gradient (PCG) solver is used [76]. Finally, a diagonal incomplete-LU asymmetric (DILU) PCG preconditioner is used to smooth the momentum matrix, and it is solved using a preconditioned bi-conjugate gradient (PBiCG) solver [76].

3.3 Volume of fluid (VOF) implementation

For this problem, the governing equations are modeled using the VOF approach [64]. The liquid and gas phases are water and air, respectively. The volume fraction of the liquid phase is defined by $\propto$, which is obtained by the solution of the convection equation (3.3).

Advection of $\propto$:

$$\propto = 1 \qquad Liquid\ phase$$

$$0 < \propto < 1 \qquad Interface\ between\ both\ phases$$

$$\propto = 0 \qquad Air\ phase$$

The mass conservation equation:

$$\text{For the fluid phase}: \quad \frac{\partial \propto}{\partial t} + \nabla(\propto v_l) = 0 \tag{3.4}$$

$$\text{For the air phase:} \quad \frac{\partial \propto}{\partial t} + \nabla((1-\propto)v_a) = 0 \tag{3.5}$$

where v_l is the velocity of the liquid, v_a is the velocity of the air and $\propto_a = (1-\propto)$ is the volume fraction of the air phase.

This convection equation is modified to ensure boundedness and conservation for the given problem using

$$\frac{\partial \propto}{\partial t} + \nabla.(\propto V) + \nabla.((1-\propto) \propto v_r) = 0 \tag{3.6}$$

where v_r is the velocity of the interface, and the additional term represents the compression term, which is active only near the interface and can significantly reduce the dissipation between the two phases while using the VOF method. Berberovic *et al.* [73] stated that the relative velocity at a cell face depends on the phase fraction, the velocity over the face, and the maximum velocity magnitude in the region between the two phases.

3.4 Model for contact line motion

In interFoam, the effects of surface tension are incorporated by the inclusion of a body force term in the momentum equation (3.2). Among the effects of the surface tension at the interface is the generation of a phase gradient between the phases, which is accounted for via f_b, which is the body force term determined with the continuum surface force model of Brackbill *et al.* [72]

$$f_b = \sigma[-\nabla\left(\frac{\nabla \propto}{|\nabla \propto|}\right)]\nabla \propto \tag{3.7}$$

where σ is the surface tension, $\frac{\nabla \propto}{|\nabla \propto|}$ represents the normal to the interface and $[-\nabla\left(\frac{\nabla \propto}{|\nabla \propto|}\right)]$ is the curvature of the interface. For this purpose, it is crucial to compute the effects in the near-wall region using a modification to account for the contact angle:

$$\left(\frac{\nabla\propto}{|\nabla\propto|}\right)_{mod} = n_{wall}cos\theta + t_{wall}sin\theta \quad (3.8)$$

where θ is the contact angle, which must be obtained from experimental data, n_{wall} is the normal to the wall and t_{wall} is the tangent to the wall.

interFoam calculates the dynamic contact angle using the following equation:

$$\theta = \theta_0 + (\theta_A - \theta_R) \times \tanh(\frac{u_{wall}}{u_\theta}) \quad (3.9)$$

where θ_0 is the static contact angle, θ_A is the advancing angle, θ_R is the receding angle, $(\theta_A - \theta_R)$ is the contact angle hysteresis, u_{wall} is an approximation of the velocity of the contact line based on the velocity of the fluid parallel to the wall near to the fluid-gas interface and the parameter u_θ is responsible for the rapidity of the evolution. A positive quantity indicates that it is an advancing contact line.

However, Sikalo *et al.* [77] stated that the velocity of the fluid present in an area near the wall is not equivalent to the velocity of the contact line. Logically, the hyperbolic tangent function will evolve smoothly between the advancing angle θ_A and the receding angle θ_R whilst using the static contact angle (SCA) at $u_{wall} = 0$.

The problem posed by the previous equation (3.9) is that it cannot return the advancing or the receding contact angles at its extremes. To resolve this matter, a modified equation was implemented in interFoam [78]

$$\theta = \theta_0 + (\theta_A - \theta_R) \times \tanh(\frac{u_{wall}+|u_{wall}|}{2u_\theta}) + (\theta_R - \theta_0) \times \tanh(\frac{u_{wall}-|u_{wall}|}{2u_{wall}}). \quad (3.10)$$

In equation (3.10), when u_{wall} is positive, representing an advancing contact line, the last hyperbolic tangent function is 0 and $\theta = \theta_A$. In the same way, when u_{wall} returns a negative value, it represents a receding contact line, and the first hyperbolic function is 0 and $\theta = \theta_R$. However, the results predicted by both equation (3.9) and

(3.10) did not exhibit significant differences; therefore, the original version implemented in OpenFOAM equation (3.9) was employed in this study.

CHAPTER IV

RESULTS

4.1 Presentation of the cases

Three-dimensional simulations were performed using the CFD code OpenFOAM. The VOF method was employed to simulate two fluids, air and water, represented by a

50 μm-diameter droplet located at 57.5 μm above the surface. The aim of the simulations is the analysis of droplet impact at a speed of 60 m/s on superhydrophobic surfaces with micro-scale roughness elements (MRE) and to establish whether the MRE enhance the hydrophicity of a surface or not. Three simulations were generated: the first one was a droplet impacting a smooth superhydrophobic surface which served as a control, the second was a droplet impacting a superhydrophobic surface with anisotropic MREs and the third a droplet impacting a superhydrophobic surface with isotropic MREs.

The computational domains used for the simulations were generated using the OpenFOAM utilities blockMesh, mergeMeshes, stitchMesh and transformPoints [14]. The dimensions of the three Cartesian meshes were respectively 230 μm x 230 μm x 230 μm (Figure 4.1), 240 μm x 230 μm x 230 μm, (Figure 4.2) and 235 μm x 230 μm x 245 μm (Figure 4.3).

The MREs for the second case, which can best be described as “channels,” are considered anisotropic because of their size 5 μm x 5 μm x 230 μm and shape. This

configuration was chosen to mimic the anisotropic structures on the strider leg (Figure 2.3) and the duck feather (Figure 2.4B). No attempt was made to match the physical dimensions of these structures. There are 23 such channels in the computational domain. Regarding the third case, (Figure 4.4) shows three fundamental elements that were used to create the computational domain: a cube, a half cube and a quarter cube. These latter formed "cubic posts" of 5 μm x 5 μm x 5 μm that were used along with OpenFOAM utilities to create an isotropic configuration of 600 cubic MREs for the third case. The spacing between each post was 5 μm. This configuration was chosen to mimic the isotropic structures on the mosquito eye (Figure 2.4 A) and the lotus leaf (Figure 2.5 A). As before, no attempt was made to match the physical dimensions of these structures.

Results from a previous study conducted by Burtnett [69] using axisymmetric simulations were inconclusive regarding the effectiveness of MREs for high-speed droplet impact. To that end, this investigation used three-dimensional domains that were discretized using Cartesian meshes. These latter were isotropically refined basing the mesh point spacing on the previous axisymmetric simulations done by Burtnett [69]. The refinement of the Cartesian meshes defined three regions with different resolutions. The first region was a coarse area characterized by 10 cells per radius (CPR), based on the radius of the droplet, the second region, which included the droplet in its initial position, was 40 (CPR) and the finest grid, which included the region near the wall, had a spacing of 80 (CPR), see (Figure 4.5). In total, the domains contained approximately 66M to 73M elements, depending on the case.

In order to reduce simulation time, the three-dimensional simulations were performed using a quarter-plane symmetry in which the two symmetry planes intersect

along the vertical axis of the droplet. The jobs were executed on Shadow at the Mississippi State University (MSU) High Performance Computing Collaboratory (HPCC), which is a Cray CS300-LC cluster with 4800 Intel Ivy Bridge processor cores and 28,800 Intel Xeon Phi cores. Each node has either 512 GB of RAM (45%), 128 GB of RAM (45%) or 64 GB of RAM (10%) for a system total of 70 TB of RAM. Shadow has a peak performance of 593 teraFLOPS (trillion calculations per second) and is one of the fastest, energy efficient and powerful computer in the world [78].

HPCC policies allow a minimum of 200 processors per job and that is the number of processors used to generate each one of the three simulations. A lot of efforts was made to reduce their computational cost; unfortunately, these attempts did not greatly impact their computational time. In fact, each simulation has unique surface characteristics that lead the fluid to flow differently and eventually caused the computational time to vary for each case (Table 4.1).

Table 4.1 Computational time recorded for each case

Case	Number of elements	Number of MREs	Computational time (hr)
1	67,669,680	N/A	528
2	66,089,856	23	864
3	72,664,256	600	1008

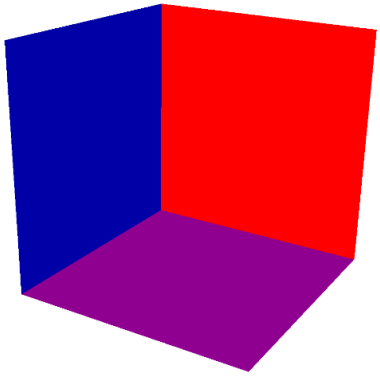

Figure 4.1 Domain of the first simulation - CASE I –

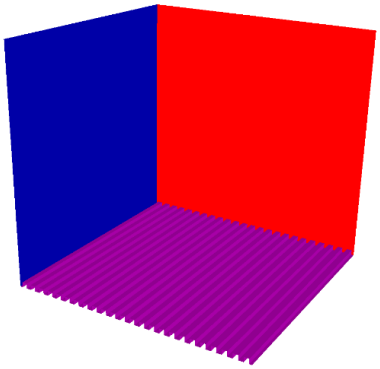

Figure 4.2 Domain of the second simulation - CASE II –

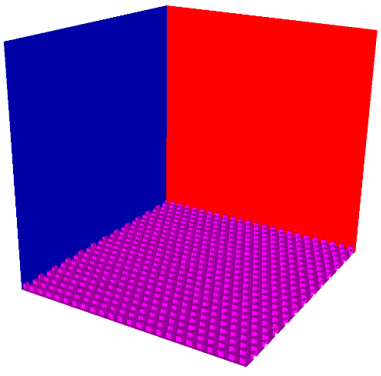

Figure 4.3 Domain of the third simulation - CASE III –

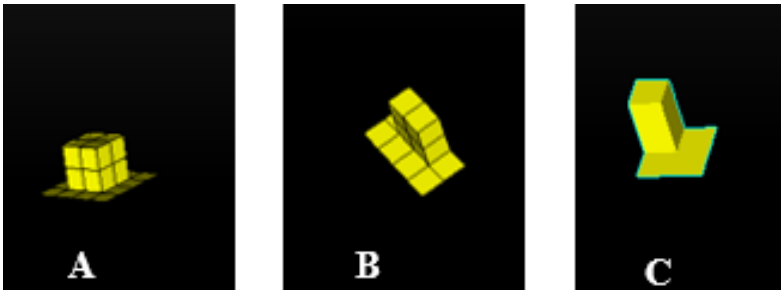

Figure 4.4 Fundamental components of the MRE used for the composition of the domain (CASE III)

A-cube , B-half a cube , C-quarter of a cube

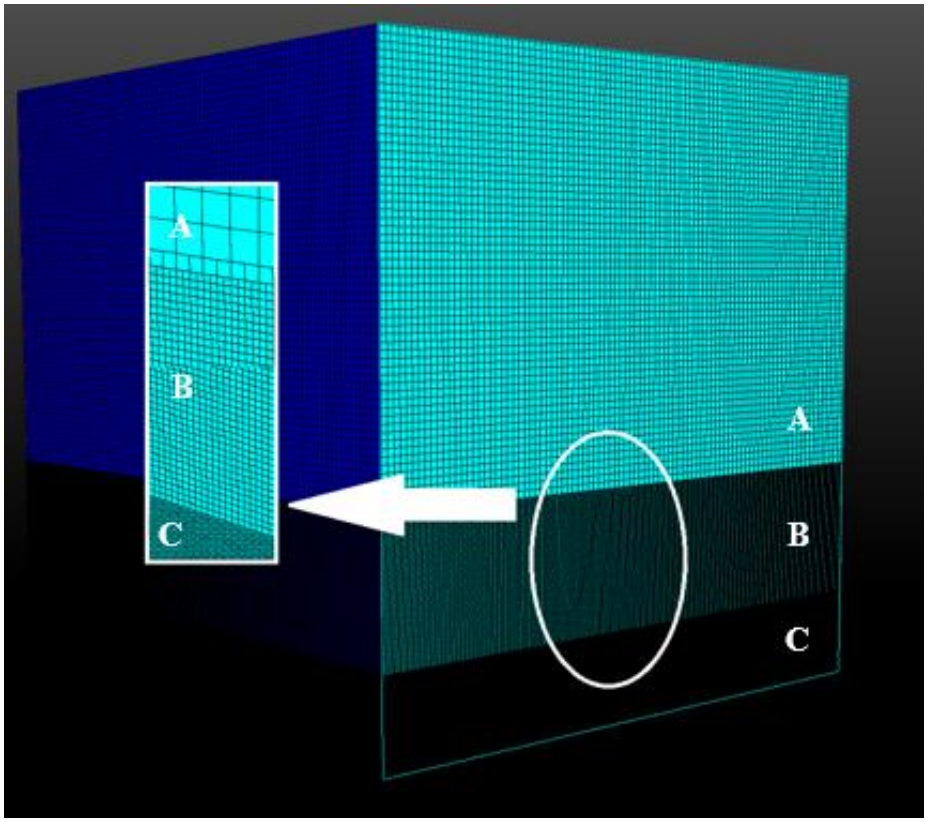

Figure 4.5 Refined Domain

A-10 CPR ; B-40 CPR; C-80 CPR

4.2 Boundary conditions

The six boundary patches generated by the blockMesh utility are: *leftWall*, *rightWall*, *lowerWall*, *atmosphere, frontWall* and *backWall* (Figure 4.6). As the simulations were performed on only one quarter of the domain, two of the patches (*rightWall* and *backWall*) were defined as symmetryPlane to simulate a full domain. In contrast, the two remaining patches (*frontWall and leftWall)* were designated as a zeroGradient type, which forces the gradients of velocity, pressure, and alpha.water, normal to the boundary to be zero.

The patch *atmosphere*, which is the top boundary, must allow both outflow and inflow. Therefore, in order to permit this while preserving stability, the following boundary conditions have been set for the velocity, pressure and alpha.water:

- For velocity: pressureInletOutletVelocity, which applies zeroGradient on all components, except where there is inflow, in which case a fixedValue condition is applied to the tangential component in other words it switches U and P between fixedValue and zeroGradient depending on direction of U [79].
- For pressure: totalPressure which is a fixedValue condition calculated from specified total pressure $P_o = p + \frac{1}{2}\rho\,|\mathrm{U}|^2$. When U changes, P is adjusted accordingly [79].
- For alpha.water: inletOutlet, is a zeroGradient condition when flow is outward and a fixedValue when flow is inward [79].

Concerning the last boundary patch, the *lowerWall* was defined as a no-slip wall in the boundary file. Since this problem should contain a lower boundary that accounts

for the effects of surface tension between the wall, and the interface, the boundary condition of the *lowerWall* was set accordingly. Actually, the interFoam solver includes the modelling of the effects of surface tension that are applied by specifying the alphaContactAngle boundary condition on alpha.water and pressure's boundaryfield along with setting the following special numerical values for this investigation: the static contact angle to $\theta_0 = 149$, the velocity scaling function to $U_\theta = 0.01$, and leading and trailing edge dynamic contact angles, $\theta_A = 154$ and $\theta_R = 150$ respectively.

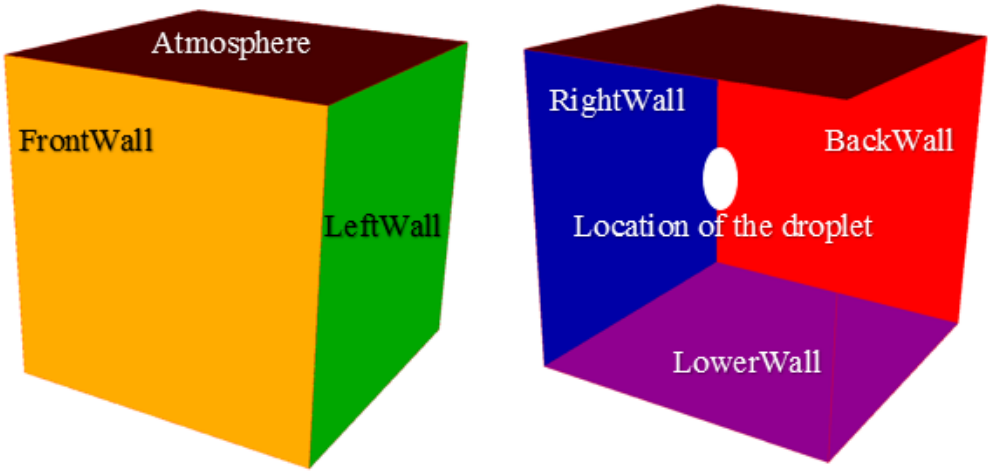

Figure 4.6 Boundary patches & location of the droplet

4.3 Case I - Dry, smooth superhydrophobic surface

The first case represents the impact of a droplet on a dry, smooth superhydrophobic surface at a speed of 60 m/s (Figure 4.7). This case is used as a control in order to evaluate the effectiveness of the MREs. In reality, this superhydrophobic surface would include both a chemical treatment applied to the surface to reduce surface energy and the nanoscale roughness on the surface. However, this case was designated as

smooth since this simulation was performed at a microscopic scale and that nanoscale effects were modeled through the contact angle.

The simulation showed that once the droplet impacted the surface, it splashed (Figure 4.8) and produced satellite droplets and droplet fingering (Figure 4.9). The phase evolution of the droplet impact captured by the simulation showed that the splash produced a few residual droplets that were dispersed over the surface (Figure 4.10). At a time of 10μs after droplet impact, the fluid began to retract from its maximum spread and a receding break up occurred. After a time of 13 μs, the fluid retraction showed the beginning of a complete rebound and an attempt to regain its initial shape (Figure 4.11). From the latest phase depicted by the simulation, it was observed that the behavior of droplet impact at high speed on dry, smooth superhydrophobic surface was as desired. In fact, a significant amount of the fluid approximately regained its initial shape and rebounded off the surface leaving only a negligible amount of satellite droplets (Figure 4.12).

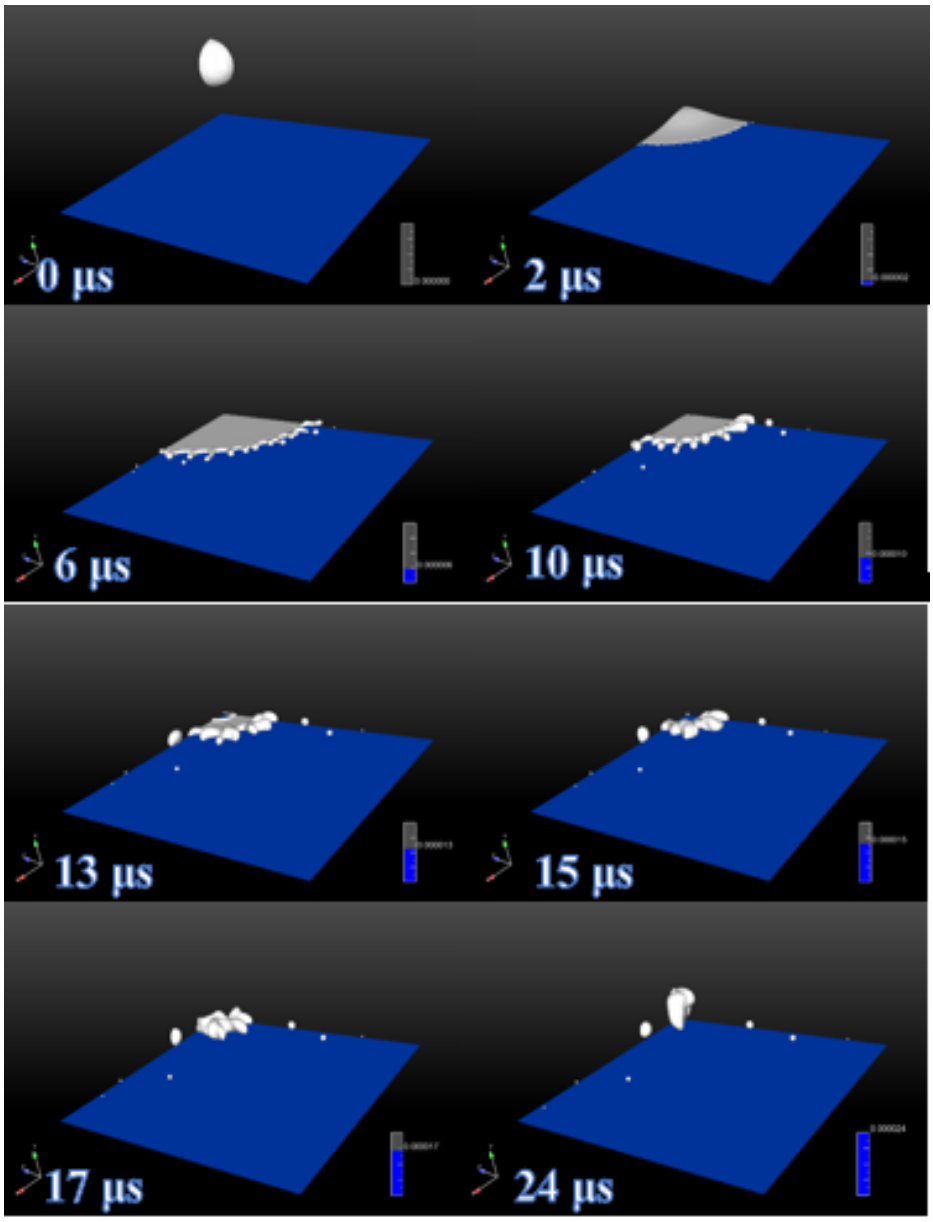

Figure 4.7 Simulation of Case I – Evolution phases of droplet impact on dry, smooth superhydrophobic surface

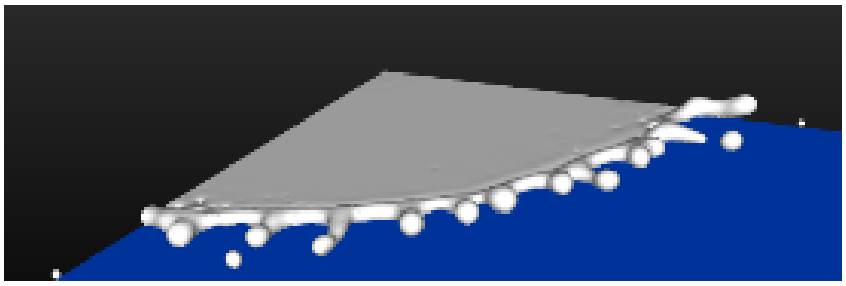

Figure 4.8 Droplet Splash

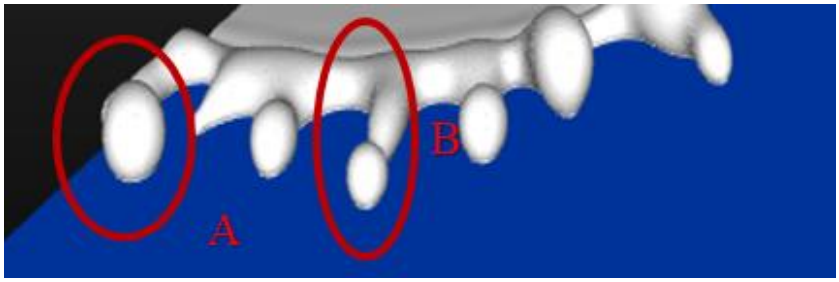

Figure 4.9 A: Satellite droplet, B: Droplet fingering

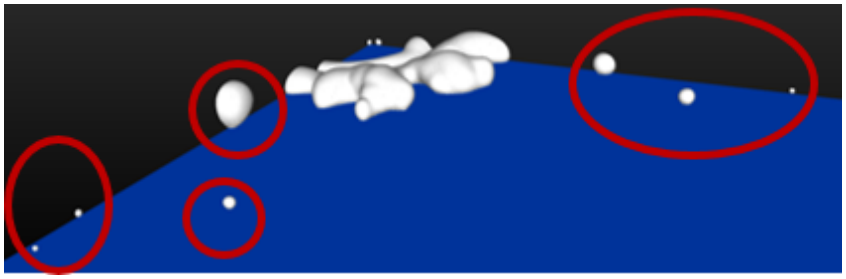

Figure 4.10 Residual droplets

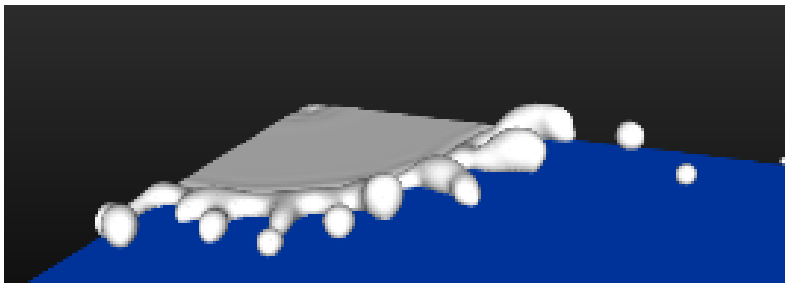

Figure 4.11 Receding breakup

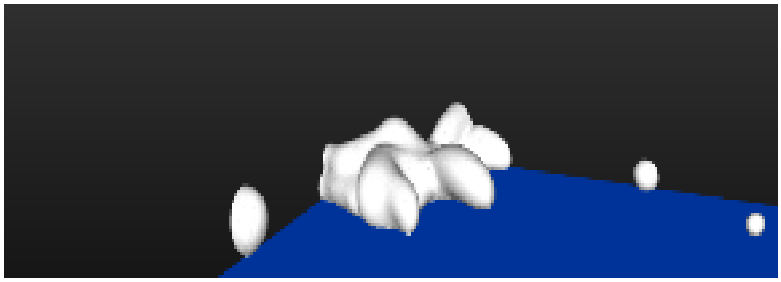

Figure 4.12 Retraction of the fluid

Figure 4.13 Droplet rebound

4.4 Case II - Dry, superhydrophobic surface with anisotropic micro-scale roughness elements

For this case, the droplet impacted a dry, superhydrophobic surface with anisotropic MREs at a speed of 60 m/s. The anisotropic MREs of 5 μm x 5 μm x 230 μm form a surface of 23 channels (Figure 4.14).

Once the droplet impacts the surface, it breaks and produces a prompt splash. The splashing generates several satellite droplets (figure 4.15) and droplet fingering (Figure 4.16). At a time of 4 μs after the droplet impact, the fluid flowing through the surface starts to adapt to the shape of the channels creating several patterns (Figure 4.17). After 6 μs from the beginning of the simulation, some of the residual droplets vacate the domain while others get trapped between the MREs. By the last time step, no significant changes were observed. A significant amount of the fluid was still obstructed by the MREs whereas the remnants of the droplets rebounded off the surface and scattered all over the domain.

This simulation showed that the anisotropic configuration of the MREs caused the rebound of the droplets to be poorly defined (Figure 4.18). Moreover, it proved, by the amount of fluid left on the surface, that these anisotropic MREs are not effective for high-speed impacts.

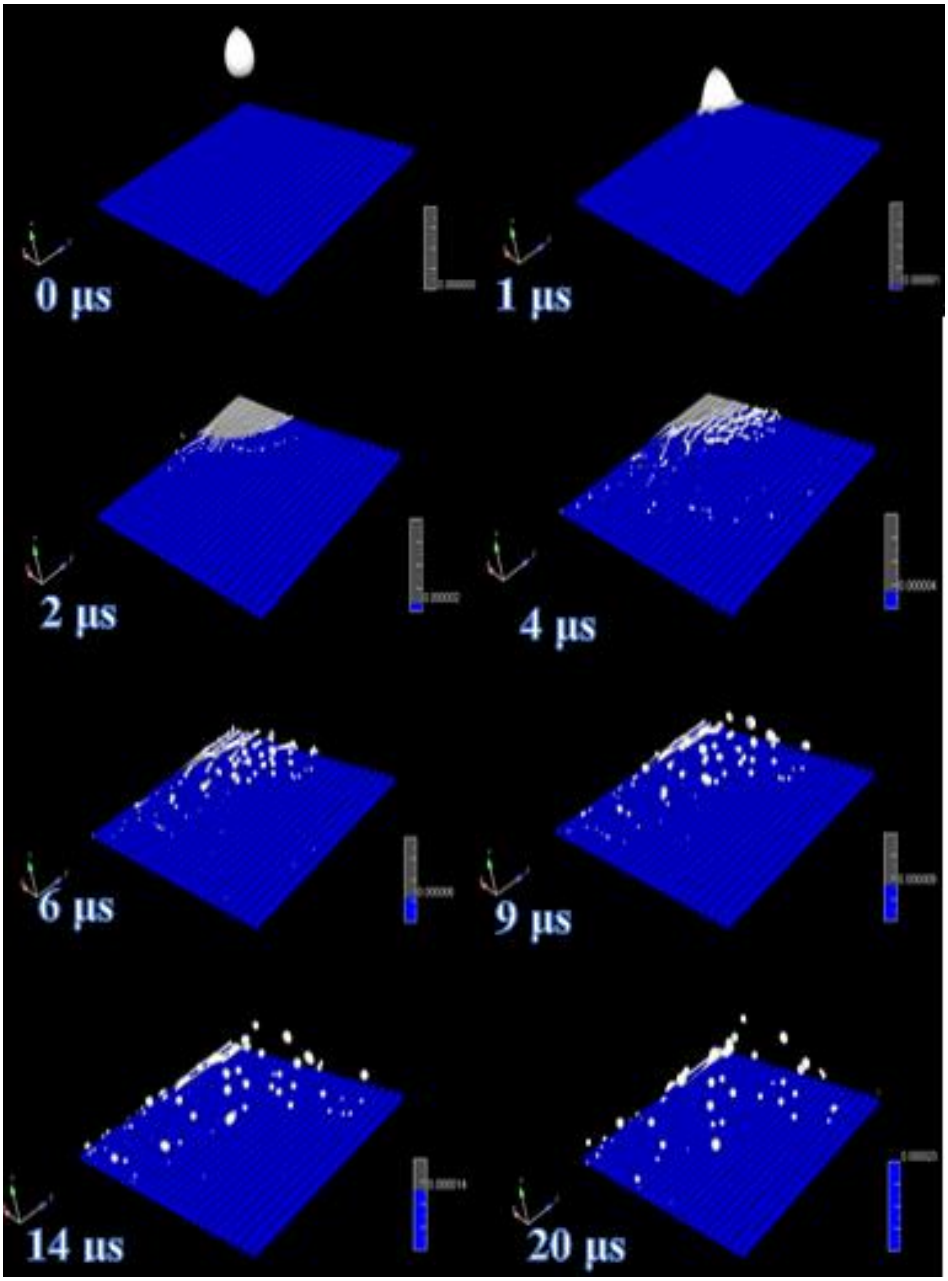

Figure 4.14 Simulation of Case II – Evolution phases of droplet impact on dry superhydrophobic surface with anisotropic MRE configuration

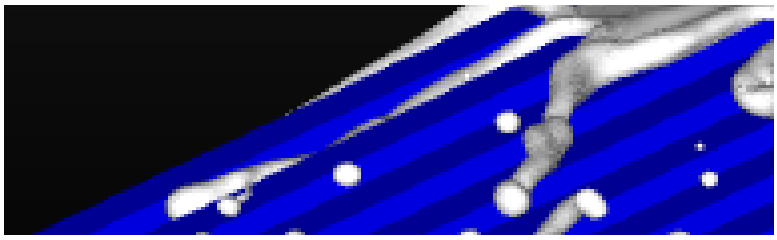

Figure 4.15 Droplet Fingering

Figure 4.16 Satellite droplets

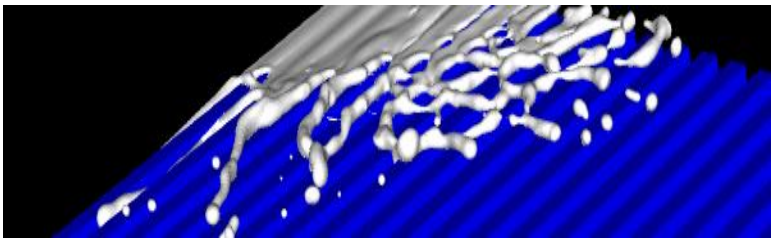

Figure 4.17 Fluid flow patterns

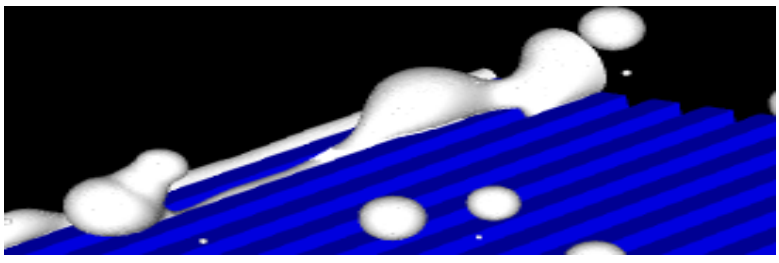

Figure 4.18 Incomplete rebound

4.5 Case III - Dry, superhydrophobic surface with isotropic micro-scale roughness elements

The simulation for the third case involved the impact of a droplet on a dry, superhydrophobic surface with isotropic MREs at the same speed as the two previous simulations (Figure 4.19). There are 600 MREs, shaped as cubic posts with dimension 5 μm x 5 μm x 5 μm, on the surface.

The simulation showed that, when the droplet impacted the surface, it brutally burst and produced a prompt splash . Subsequently, the prompt splash caused the creation of various droplet fingers and satellite droplets (Figure 4.20). Due to the small size and the very large number of cubic posts present on the surface, it was observed that numerous residual droplets were scattered over the surface causing some of them to exit the domain (Figure 4.21). In addition, at a time of 4 μs after the droplet impact, some complex patterns started to form. This was mainly due to the fluid flowing in between the MRE cavities (Figure 4.22). Eventually, at the end of the simulation, some of the fluid retracted and bounced off the surface whereas some of it remained trapped between the cubic posts (Figure 4.23).

By the effects stated previously, it was established that this simulation demonstrated the relative ineffectiveness of the MREs present on the dry superhydrophobic surface subjected to high speed droplet impact. Indeed, this case exhibited that the MREs shape, size and configuration were the main cause of the significant amount of fluid left on the surface and the producation of satellite droplets.

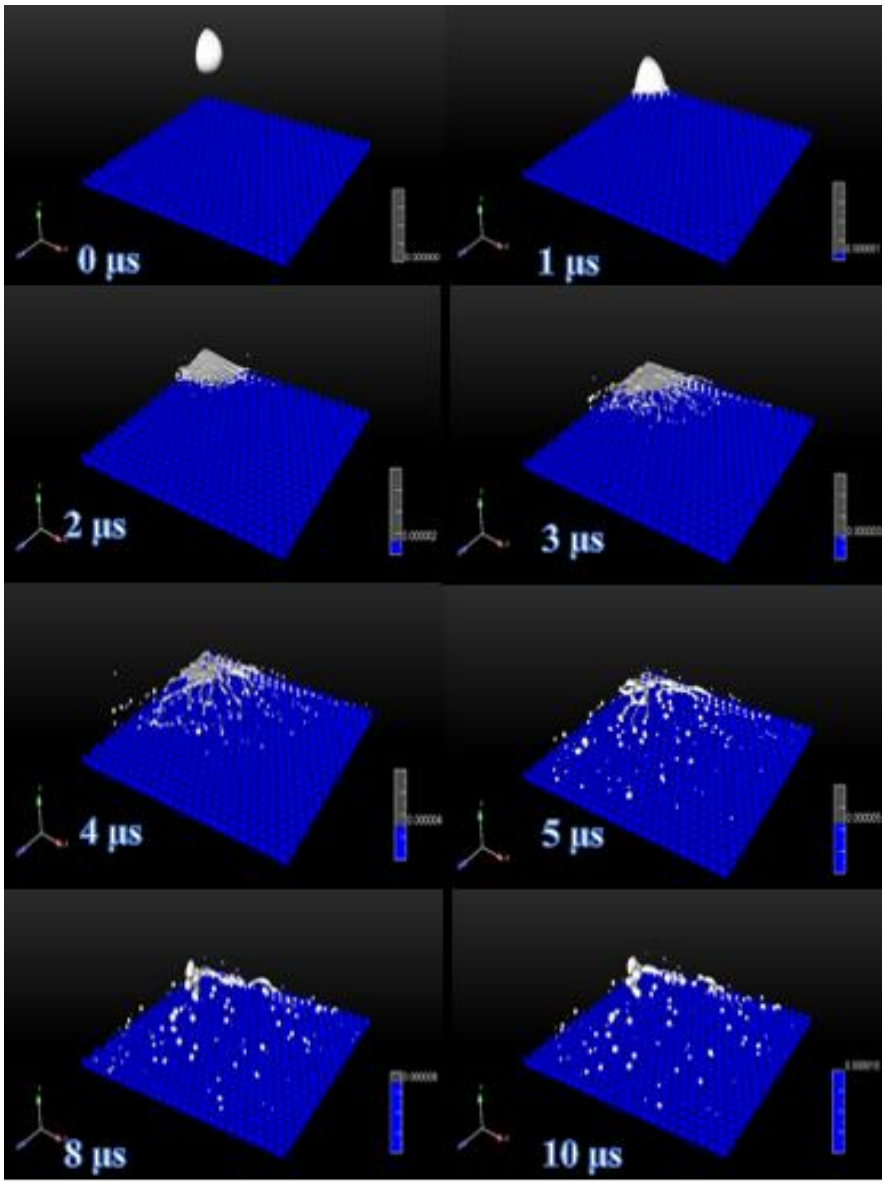

Figure 4.19 Simulation of Case III – Evolution phases of droplet impact on dry superhydrophobic surface with isotropic MRE configuration

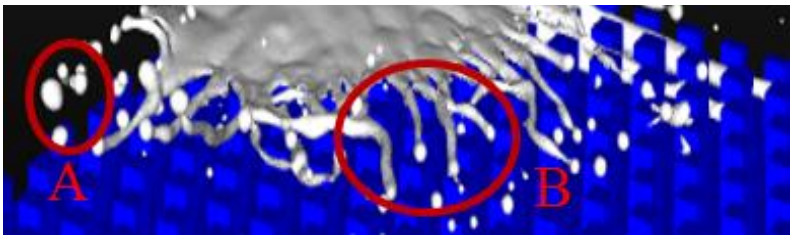

Figure 4.20 A:Satellite droplets, B: Droplet fingering

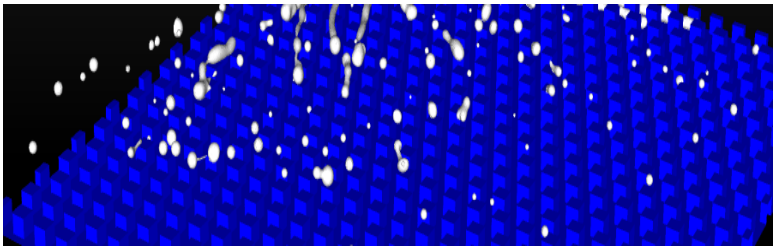

Figure 4.21 Residual droplets

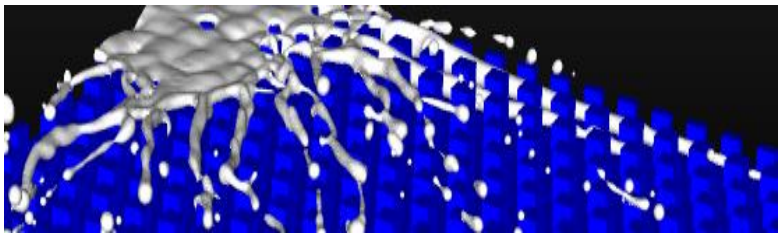

Figure 4.22 Complex fluid flow patterns

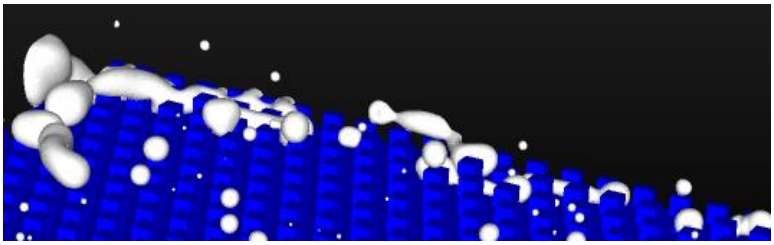

Figure 4.23 Fluid trapped by the cubic posts

CHAPTER V

CONCLUSIONS

The three simulations, in which a 50 μm diameter droplet impacts a surface at 60 m/s, showed that the water repellent characteristics of dry superhydrophobic surfaces are apparent. In each case, the droplets bounced off the surface, to varying degrees, after impact. However, when comparing these cases, significant differences were observed.

Only a few satellite droplets stayed on the smooth superhydrophobic surface, while the remaining fluid rebounded off the surface and returned to its initial shape. In contrast, the superhydrophobic surface with the anisotropic, channel-like MRE configuration caused the droplet to shatter into several satellite droplets with some fluid remaining trapped in the channels. The third surface, with isotropic cubic MREs, produced the largest number of residual droplets after the impact due to the small size and large number of posts present on the surface. Similar to the second simulation, the third simulation showed that the fluid spreads through the domain and eventually, due to a channeling effect, takes the shape of the cavities present between the cubic posts.

The videos and images of the simulations demonstrated that the structured MREs were inefficient in enhancing the hydrophobicity of a surface for a droplet impacting the surface at high speed. The specific configuration of the MREs, either isotropic or anisotropic, did not improve the behavior of droplet impact on superhydrophic surface. Nevertheless, this research exhibits that the presence of numerous small MREs on the

surface causes the worst comportment of the droplet, where it breaks apart and leaves a significant number of residual droplets, fingering droplets, and fluid in the domain. However, this study considered only two MRE configurations.

For future work, a grid refinement study should be performed to establish if the behavior of the droplet seen on these simulations was numerically or physically induced. Although the point spacing in the grid was based on previous axisymmetric simulations, its appropriateness for three-dimensional simulations has not been established. Furthermore, it would be necessary to do an experimental investigation to gather data in order to validate the results for both dry, superhydrophobic surfaces with anisotropic and isotropic simulations. In addition, three-dimensional simulations that included freezing would be appropriate to determine if the satellite droplets solidify after impact rather than return to the surface. Additionally, the use of high performance computational resources is highly recommended to ensure the reduction of the computational time and cost.

REFERENCES

[1] Office of Aviation Safety Aircraft Icing Accidents Donald Eick- NTSB Senior Meteorologist Presentation to NCAR In-Flight Icing Users Technical Interchange.-Documents-Online Powerpoint Presentation and Document Sharinf-*Docfoc.com* .N.p.,(2015).

[2] FAA, U. D. O. T., NSP GB National Simulator Program FSTD Qualification Guidance Bulletin FAA, U. (2016). *NSP GB National Simulator Program FSTD Qualification Guidance Bulletin*. [PDF] Washington, DC: FAA, p.1. Available at: https://www.faa.gov/about/initiatives/nsp/bulletins/media/11-04.pdf.

[3] Jeck, R. K. (2002). *Icing Design Envelopes (14 CFR Parts 25 and 29, Appenddix C) Converted to a Distance-Based Format* (No. DOT/FAA/AR-00/30). FEDERAL AVIATION ADMINISTRATION TECHNICAL CENTER ATLANTIC CITY NJ.

[4] Thomas, S. K., Cassoni, R. P., & MacArthur, C. D. (1996). Aircraft anti-icing and de-icing techniques and modeling. *Journal of Aircraft*, *33*(5), 841-854.

[5] Sloan, Jeff. "787 Integrates New Composite Wing Deicing System: Compositesworld". *Compositesworld.com*. Retrieved from: http://www.compositesworld.com/articles/787-integrates-new-composite-wing-deicing-system.

[6] Kim, P., Wong, T., Alvarenga, J., Kreder, M. J., Adorno-Martinez, W. E. ET Aizenberg, J. "Liquid-Infused Nanostructured Surfaces with Extreme Anti-Ice and Anti-Frost Performance". *ACS Nano* 6.8 (2012): 6569-6577.

[7] "Deicing and Anti-Icing Unite". NASA STI. 2002.Retrived from: https://spinoff.nasa.gov/spinoff2002/ps_1.html

[8] "Flight April | April Iith | Fluid System | 1946 | 0710 | Flight Archive". Retrieved from : https://www.flightglobal.com/pdfarchive/view/1946/1946%20-%200710.html

[9] TKS Ice Protection - Plane & Pilot Magazine". *Plane & Pilot Magazine*. Retrieved from: http://www.planeandpilotmag.com/article/tks-ice protection/

[10] Strobl, T., Storm, S., Thompson, D., Hornung, M., & Thielecke, F. (2015). Feasibility study of a hybrid Ice protection system. Journal of Aircraft, 52(6), 2064-2076.

[11] "Aircraft Accident Report of the 9th july 1996 -AMERICAN EAGLE FLIGHT 4184"". *Libraryonline*. Retrieved from: http://libraryonline.erau.edu/online-full-text/ntsb/aircraft-accident-reports/AAR96-01.pdf

[12] "Fatal Mali MD-83 Accident Blamed on Engine Icing and Lack of Stall Recovery". *ASN News*. Retrieved from: http://news.aviation-safety.net/2016/04/23/fatal-mali-md-83-accident-blamed-on-engine-icing-and-lack-of-stall-recovery.

[13] Ranter, H. "ASN Aircraft Accident IRMA/Britten-Norman BN-2A-27 Islander YR-BNP Petreasa, Alba". *Aviation-safety.net*. Retrieved from: https://aviation-safety.net/database/record.php?id=20140120-0.

[14] Mishchenko, L., Hatton, B., Bahadur, V., Taylor, J. A., Krupenkin, T., & Aizenberg, J. (2010). Design of ice-free nanostructured surfaces based on repulsion of impacting water droplets. *ACS nano*, *4*(12), 7699-7707.

[15] "Openfoam". *OpenFOAM documentation, User Guide*. Retrievied from: http://www.openfoam.com/docts/user

[16] "Ensight 10.1 New Release". *EnSight*. Retrieved from: https://www.ensight.com/ensight-10-1/

[17] "Paraview". *Paraview.org*. Retrieved from : http://www.paraview.org/

[18] Rioboo, R., Marengo, M., & Tropea, C. (2001). Outcomes of a Drop Impact on Solid Surface. *Atomization and Sprays, 11* (2), 155-65.

[19] Hansen, F. K. (2004). The measurement of surface energy of polymers by means of contact angles of liquids on solid surfaces. *A short overview of frequently used methods. University of Oslo, Oslo*.

[20] Rioboo, R., Marengo, M., & Tropea, C. (2002). Time evolution of liquid drop impact onto solid, dry surfaces. *Experiments in Fluids*, *33*(1), 112-124.

[21] Yarin, A. L. (2006). Drop impact dynamics: splashing, spreading, receding, bouncing…. *Annu. Rev. Fluid Mech.*, 38, 159-192

[22] Marmur, A. (2013). Superhydrophobic and superhygrophobic surfaces: from understanding non-wettability to design considerations. Soft Matter, 9(33), 7900-7904.

[23] Drelich, J., Chibowski, E., Meng, D. D., & Terpilowski, K. (2011). Hydrophilic and superhydrophilic surfaces and materials. *Soft Matter*, *7*(21), 9804-9828.

[24] Gao, X. F.; Jiang, L. (2004). Water-Repellent Legs of Water Striders. *Nature*, 432, 36.

[25] Leg of a strider. Retrieved from: www.savageimageaward.wordpress.com

[26] Gao, X. F.; Yan, X.; Yao, X.; Xu, L.; Zhang, K.; Zhang, J. H.; Yang, B.; Jiang, L. (2007). The Dry-Style Antifogging Properties of Mosquito Compound Eyes and Artificial Analogues Prepared by Soft Lithography. *Adv. Mater.* 19, 2213–2217.

[27] Liu, Y., Chen, X., & Xin, J. H. (2008). Hydrophobic duck feathers and their simulation on textile substrates for water repellent treatment. Bioinspiration & biomimetics, 3(4), 046007.

[28] Eye of a mosquito. Retrived from: https://www.quora.com/How-many-eyes-does-a-moquito-have

[29] Water drops on duck's feather. Retrived from: https://motherwit.wordpress.com/2010/02/07/more-feather-art/

[30] Guo, Z., Weimin, L., & Bao-Lian, S. (2011). Superhydrohobic surfaces: From natural to biomimetic to functional. *Journal of Colloid and Interface Science*. 353, 335-355.

[31] Feng, L., Zhang, Y., Xi, J., Zhu, Y., Wang, N., Xia, F., & Jiang, L. (2008). Petal effect: a superhydrophobic state with high adhesive force. Langmuir, 24(8), 4114-4119.

[32] Thielicke,W.. Computer graphic of a lotus leaf surface. Retrieved from: http://wthielicke.gmxhome.de/bionik/indexuk.htm

[33] The Petal effect. Retrieved from: http://www.care2.com/news/member/101900347/717536

[34] Scheer, B. W., & Stover, J. C. (1997, September). Development of a smooth-surface microroughness standard. In Optical Science, Engineering and Instrumentation'97 (pp. 78-87). International Society for Optics and Photonics.

[35] Yoshimitsu, Z., Nakajima, A., Watanabe, T., & Hashimoto, K. (2002). Effects of surface structure on the hydrophobicity and sliding behavior of water droplets.*Langmuir*, *18*(15), 5818-5822.

[36] Patankar, N. A. (2004). Transition between superhydrophobic states on rough surfaces. *Langmuir*, *20*(17), 7097-7102.

[37] Heydari, G., Thormann, E., Järn, M., Tyrode, E., & Claesson, P. M. (2013). Hydrophobic surfaces: topography effects on wetting by supercooled water and freezing delay. *The Journal of Physical Chemistry C*, *117*(42), 21752-21762.

[38] Jung, S., Tiwari, M. K., Doan, N. V., & Poulikakos, D. (2012). Mechanism of supercooled droplet freezing on surfaces. *Nature communications*, *3*, 615.

[39] Worthington, A. M. (1876). On the forms assumed by drops of liquids falling vertically on a horizontal plate. *Proceedings of the royal society of London*, *25*(171-178), 261-272.

[40] Worthington, A. M. (1876). A Second Paper on the Forms Assumed by Drops of Liquids Falling Vertically on a Horizontal Plate. *Proceedings of the Royal Society of London*, *25*(171-178), 498-503.

[41] Worthington, A. M. (1907). *The splash of a drop*. Society for Promoting Christian Knowledge.

[42] Engel, O. G. (1955). Waterdrop collisions with solid surfaces. *Journal of Research of the National Bureau of Standards*, *54*(5), 281-298.

[43] Levin, Z., & Hobbs, P. V. (1971). Splashing of water drops on solid and wetted surfaces: hydrodynamics and charge separation. *Philosophical Transactions of the Royal Society of London A: Mathematical, Physical and Engineering Sciences*, *269*(1200), 555-585.

[44] Stow, C. D., & Hadfield, M. G. (1981, January). An experimental investigation of fluid flow resulting from the impact of a water drop with an unyielding dry surface. In *Proceedings of the Royal Society of London A: Mathematical, Physical and Engineering Sciences* (Vol. 373, No. 1755, pp. 419-441). The Royal Society.

[45] Mundo, C. H. R., Sommerfeld, M., & Tropea, C. (1995). Droplet-wall collisions: experimental studies of the deformation and breakup process. *International journal of multiphase flow*, *21*(2), 151-173.

[46] Yarin, A. L., & Weiss, D. A. (1995). Impact of drops on solid surfaces: self-similar capillary waves, and splashing as a new type of kinematic discontinuity.*Journal of Fluid Mechanics*, *283*, 141-173.

[47] Cossali, G. E., Coghe, A., & Marengo, M. (1997). The impact of a single drop on a wetted solid surface. *Experiments in fluids*, *22*(6), 463-472.

[48] Wachters, L. H. J., & Westerling, N. A. J. (1966). The heat transfer from a hot wall to impinging water drops in the spheroidal state. *Chemical Engineering Science*, *21*(11), 1047-1056.

[49] Range, K., & Feuillebois, F. (1998). Influence of surface roughness on liquid drop impact. *Journal of Colloid and Interface Science*, *203*(1), 16-30.

[50] Allen, R. F. (1975). The role of surface tension in splashing. *Journal of colloid and interface science*, *51*(2), 350-351.

[51] Sharp, D. H. (1984). An overview of Rayleigh-Taylor instability. *Physica D: Nonlinear Phenomena*, *12*(1), 3-18.

[52] Bhola, R., & Chandra, S. (1999). Parameters controlling solidification of molten wax droplets falling on a solid surface. *Journal of materials science*, *34*(19), 4883-4894.

[53] Pasandideh-Fard, M., Qiao, Y. M., Chandra, S., & Mostaghimi, J. (1996). Capillary effects during droplet impact on a solid surface. *Physics of Fluids (1994-present)*, *8*(3), 650-659.

[54] Aziz, S. D., & Chandra, S. (2000). Impact, recoil and splashing of molten metal droplets. *International journal of heat and mass transfer*, *43*(16), 2841-2857.

[55] Marmanis, H., & Thoroddsen, S. T. (1996). Scaling of the fingering pattern of an impacting drop. *Physics of Fluids (1994-present)*, *8*(6), 1344-1346.

[56] Kim, H. Y., Feng, Z. C., & Chun, J. H. (2000). Instability of a liquid jet emerging from a droplet upon collision with a solid surface. *Physics of Fluids (1994-present)*, *12*(3), 531-541.

[57] Thoroddsen, S. T., & Sakakibara, J. (1998). Evolution of the fingering pattern of an impacting drop. *Physics of Fluids (1994-present)*, *10*(6), 1359-1374.

[58] Xiao, J., Mackie, K. E., Osborne, J. H., Seebergh, J., & Chaudhuri, S. (2011).*In-Silico Environment for Designing Anti-icing Surfaces* (No. 2011-38-0001). SAE Technical Paper.

[59] Cao, L., Jones, A., Sikka, V., Wu, J., & Gao. (2009) D. Anti-Icing Superhydrophobic Coatings. *Langmuir*. 25 (21), 12444-12448.

[60] Jung, S., Dorrestijn, M., Raps, D., Das, A., Megaridis, C. M., & Poulikakos, D. (2011). Are superhydrophobic surfaces best for icephobicity?. Langmuir, 27(6), 3059-3066.

[61] Hirt, C., & Nichols, B. (1981). Volume of Fluid (VOF) Method for the Dynamics of Free Boundaries. *Journal of Computational Physics*, 39 (1), 201-225.

[62] Unverdi, S. O., & Tryggvason, G. (1992). A front tracking method for viscous incompressible, multi-fluid flows. *Journal of Computational Physics*, 100, 25-37.

[63] Shu, B., Dammel, F., & Stephan P. (2007). Implementation of the Level Set Method into OpenFOAM for Capturing the Free Interface in Incompressible Fluid Flows. (2007). *OpenFOAM International Conference.* Old Windsor, UK.

[64] Shan, X., & Chen, H. (1993) .Lattice Boltzmann model for simulating flows with multiple phases and components. *Physics Review E*, 47, 1815-1819.

[65] Le Gouez, J. M., de Jouiétte J. M., O.Put S. Rigaud. Volume of Fluid Method (VOF).*Principia R D*, Port de Brégaillon, 83507 La seyne Sur Mer.

[66] Bussmann, M., Chandra, S., & Mostaghimi, J. (2000). Modeling the splash of a droplet impacting a solid surface. *Physics of Fluids (1994-present)*, *12*(12), 3121-3132.

[67] Bussmann, M., Mostaghimi, J., & Chandra, S. (1999). On a three-dimensional volume tracking model of droplet impact. *Physics of Fluids (1994-present)*, *11*(6), 1406-1417.

[68] Gunjal, P., Ranade, V., & Chaudhari, R. (2005). Dynamics of Drop Impact on Solid Surface: Experiments and VOF Simulations. *AIChE Journal, 51* (1), 59-79.

[69] Burtnett E.N. (2012). Volume of fluid simulations for droplet impact on dry and wetted hydrophobic and superhydrophobic surfaces (*Master's Thesis*). Retrieved from http://sun.library.msstate.edu/ETD-db/theses/available/etd-05162012-152431/

[70] Rusche, H. (2002). Computational Fluid Dynamics of Dispersed Two-Phase Flows at High Phase Fractions. London, UK: Imperial College of Science, Technology, and Medicine.

[71] *OpenCFD Ltd.* (n.d.). Retrieved from http://www.opencfd.co.uk

[72] Brackbill, J. U., Kothe, D. B., & Zemach, C. (1992). A continuum method for modeling surface tension. *Journal of computational physics*, *100*(2), 335-354.

[73] Berberovic, E., van Hinsberg, N., Jakirlic, S., Roisman, I., & Tropea, C.(2009). Droplet Impact onto a Liquid Layer of Finite Thickness: Dynamics of the Cavity Evolution. *Physical Review E, 79* (3), 036306-1-036306-15.

[74] Issa, R. (1986). Solution of the Implicitly Discretised Fluid Flow Equations by Operator-Splitting. *Journal of Computational Physics, 62* (1), 40-65.

[75] Openfoam.org. 2014. *OpenFOAM 2.3.0: Multiphase Modelling*. Retrieved from: http://openfoam.org/release/2-3-0/multiphase/.

[76] Behrens, T. (2009). OpenFOAM's basic solvers for linear systems of equations: solvers, preconditioners, smoothers. Notes from *CFD with OpenSource Software* course, Chalmers University of Technology.

[77] Sikalo, S., Tropea, C., & Ganic, E. N. (2005). Dynamic Wetting Angle of a Spreading Droplet. *Experimental Thermal and Fluid Science, 29* (7), 795- 802.

[78] High Performance Computing at the HPC². " HPC² High Performance Computing. Retrived form: https://www.hpc.msstate.edu/computing/hpc.php

[79] "Openfoam User Guide: 5.2 Boundaries". *CFD Direct*. Retrieved from: http://cfd.direct/openfoam/user-guide/boundaries/#x24-1400252